Research in Astronomy and Astrophysics, 23:015016 (13pp), 2023 January https://doi.org/10.1088/1674-4527/aca506

Magnetic Activity and Parameters of 43 Flare Stars in the GWAC Archive

Guang-Wei Li (李广伟)[1], Chao Wu (吴潮)[1], Gui-Ping Zhou (周桂萍)[2], Chen Yang (杨晨)[3], Hua-Li Li (黎华丽)[1], Jie Chen (陈洁)[2], Li-Ping Xin (辛立平)[1], Jing Wang (王竞)[4], Hasitieer Haerken (哈斯铁尔哈尔肯)[1,5], Chao-Hong Ma (马超红)[3], Hong-Bo Cai (蔡洪波)[1], Xu-Hui Han (韩旭辉)[1], Lei Huang (黄垒)[1], Xiao-Meng Lu (卢晓猛)[1], Jian-Ying Bai (白建迎)[1], Xu-Kang Zhang (张旭康)[3], Xin-Li Hao (郝新丽)[3], Xiang-Yu Wang (王玉祥)[6,7], Zi-Gao Dai (戴子高)[6,7], En-Wei Liang (梁恩维)[4], Xiao-Feng Meng (孟小峰)[3], and Jian-Yan Wei (魏建彦)[1]

[1] Key laboratory of Space Astronomy and Technology, National Astronomical Observatories, Chinese Academy of Sciences, Beijing 100101, China; lgw@bao.ac.cn
[2] Key laboratory of Solar Activity, National Astronomical Observatories, Chinese Academy of Sciences, Beijing 100101, China
[3] Lab of Web and Mobile Data Management, Renmin University of China, Beijing 100872, China
[4] Guangxi Key Laboratory for Relativistic Astrophysics, School of Physical Science and Technology, Guangxi University, Nanning 530004, China
[5] School of Artificial Intelligence, Beijing Normal University, Beijing, 100875, China
[6] School of Astronomy and Space Science, Nanjing University, Nanjing 210093, China
[7] Key Laboratory of Modern Astronomy and Astrophysics (Nanjing University), Ministry of Education, Nanjing 210093, China
Received 2022 October 4; revised 2022 November 10; accepted 2022 November 21; published 2023 January 11

Abstract

In the archive of the Ground Wide Angle Camera (GWAC), we found 43 white light flares from 43 stars, among which, three are sympathetic or homologous flares, and one of them also has a quasi-periodic pulsation with a period of 13.0 ± 1.5 minutes. Among these 43 flare stars, there are 19 new active stars and 41 stars that have available TESS and/or K2 light curves, from which we found 931 stellar flares. We also obtained rotational or orbital periods of 34 GWAC flare stars, of which 33 are less than 5.4 days, and ephemerides of three eclipsing binaries from these light curves. Combining with low resolution spectra from LAMOST and the Xinglong 2.16 m telescope, we found that $L_{\mathrm{H}\alpha}/L_{\mathrm{bol}}$ are in the saturation region in the rotation-activity diagram. From the LAMOST medium-resolution spectrum, we found that Star #3 (HAT 178–02667) has double Hα emissions which imply it is a binary, and two components are both active stars. Thirteen stars have flare frequency distributions (FFDs) from TESS and/or K2 light curves. These FFDs show that the flares detected by GWAC can occur at a frequency of 0.5 to 9.5 yr^{-1}. The impact of flares on habitable planets was also studied based on these FFDs, and flares from some GWAC flare stars may produce enough energetic flares to destroy ozone layers, but none can trigger prebiotic chemistry on their habitable planets.

Key words: (stars:) binaries: eclipsing – stars: flare – stars: low-mass – stars: rotation

1. Introduction

Stellar flares are powerful explosions that can occur on stars ranging from A-type (Balona 2015) to even L-type (Paudel et al. 2020). Solar flares have been well studied based on space observatories, such as the Geostationary Operational Environmental Satellite (GOES), Solar Dynamics Observatory (Pesnell et al. 2012), the Reuven Ramaty High Energy Solar Spectroscopic Imager (Lin et al. 2002), and the Interface Region Imaging Spectrograph (De Pontieu et al. 2021), etc. They may release explosive energy via magnetic reconnection (Zweibel & Yamada 2009) and released by electromagnetic radiations from radio to γ-ray (e.g., Bai & Sturrock 1989; Osten et al. 2005), and coronal mass ejections (CMEs) (e.g., Kahler 1992). The stronger the flare, the more likely it is to produce a CME (Li et al. 2021). Since the Sun belongs to an ordinary inactive star of G2V type (Balona 2015), it is worthy of investigating stellar flare activities from most kinds of active stars to understand whether stellar flares may experience similar physics to solar flares or not.

Statistical studies of stellar flares have been conducted based on many survey projects. In the space, the Kepler (Borucki et al. 2010) provided photometric data with high precision, which can be used to study flare activities on stars across the H-R diagram with homogenous data for the first time (Balona 2015; Yang & Liu 2019). The Transiting Exoplanet Survey Satellite (TESS; Ricker et al. 2015) surveys all the sky, covering much wider than Kepler/K2. As a result, many new flare stars with high photometric precision can be studied (e.g., Tu et al. 2021; Howard & MacGregor 2022). On the ground, the Next Generation Transit Survey (Wheatley et al. 2018), ASAS-SN (Shappee et al. 2014), Evryscope (Law et al. 2015), and so on, have achieved fruitful results on flare study (e.g., Howard et al. 2020a; Rodríguez Martínez et al. 2020; Jackman et al. 2021).

Rotation is a key parameter to decide the activity of a star, e.g., factor in inducing stellar flares. Some indicators of stellar activity show the well-known activity-rotation relationship with a critical period. For stars with rotation periods smaller than the critical period, the activity is saturated, otherwise the activity decreases as the rotation period increases. The stellar activity-rotation relationship has been identified by X-ray (Pizzolato et al. 2003), white light (Raetz et al. 2020), Ca II H & K (Zhang et al. 2020) and Hα (Newton et al. 2017; Yang et al. 2017; Lu et al. 2019).

Pre-main sequence stars often show intense flare activities, which result in the hot plasma escaping and then angular momentum losses (Colombo et al. 2019). Magnetized stellar winds can also brake stellar rotations (Gallet & Bouvier 2013). Therefore, with rotation slowing down, flare activity decreases with age (Davenport et al. 2019; Ilin et al. 2021). The same mechanism is also proposed to occur in a close binary system (Yakut & Eggleton 2005). Magnetic braking may result in the shrink of the orbit period, and then make both components in the binary synchronously spin up (Qian et al. 2018), and thus the more frequent flare activity.

Flare activity may play key roles in affecting habitability of nearby planets in the way of UV irradiation and CMEs. For M stars, on one hand, M stars cannot produce enough UV photons (Rimmer et al. 2018), so UV radiation from frequent flares is needed to contribute to the creation of primitive life (Xu et al. 2018); on the other hand, UV radiation from frequent flares can also destroy ozone layers and life would not survive (Tilley et al. 2019). Moreover, CMEs from flares can erode even the whole atmosphere of a habitable exoplanet (Lammer et al. 2007; Atri & Mogan 2021).

In this paper, we present 43 stellar white light flares in the archive of the Ground-based Wide Angle Cameras (GWAC). GWAC is one of ground facilities of the Space-based multi-band astronomical Variable Objects Monitor (SVOM; Wei et al. 2016), in order to detect the optical transits with a cadence of 15 s (Wang et al. 2020; Xin et al. 2021). We searched all light curves during 2018 December and 2019 May of stars with Gaia G <15 mag, and found 43 stellar flares form 43 stars. In Section 2, we will introduce the light curves we used. In Section 3, we will show three sympathetic or homologous flares and one quasi-periodic pulsation. In Section 4, four binaries are studied. In Section 5, we will present the rotation-activity relationship by Hα emissions. The impacts of flares on habitable planets are discussed in Section 6. Finally, Section 7 is the conclusion.

2. Light Curves

The GWAC stellar flare candidates between 2018 December and 2019 May were obtained by the program given by Ma (2019), which tried to find flares by a wavelet algorithm. We inspected all candidates by eye and found 43 stellar flares from 43 stars. We checked these stars in SIMBAD[8] and the International Variable Star Index,[9] and found that 19 stars have never been reported as flare stars or having Hα emissions, thus new active stars. All GWAC flares are listed in Table 1. We searched their light curves from the MAST site,[10] and found TESS and K2 light curves for 39 stars. For the stars that have both K2 and TESS light curves, the TESS light curves were used. For TESS light curves, we noticed that there are several products for the same sector from different groups, and if light curves of the Science Processing Operations Center (SPOC; Jenkins et al. 2016) are available, then use them, otherwise use light curves of TESS-SPOC (Caldwell et al. 2020). The light curves of simple aperture photometry (SAP) were used, because pre-search data conditioning (PDC) ones may remove real variabilities (Vida et al. 2019). We also checked the PDC light curves of our sample, and found they work as well as SAP ones. Star #3 (HAT 178-02667), #14 (1RXS J075908.2+171957), #24, and #38 (BX Ari) have no available light curves in the MAST site. Star # 3 (HAT 178-02667) is not observed by TESS, and Star #24 is contaminated by a very bright star 13″ away. As a result, we obtained light curves of Star #14 (1RXS J075908.2+171957) and #38 (BX Ari) from their Full Frame Images. In sum, 41 of 43 GWAC flare stars have TESS or K2 light curves. The TESS sectors and K2 campaigns used in this work are listed in Table 2.

2.1. Flare Detection and Rotational Periods

To detect flares, for each light curve of a TESS sector or K2 campaign, we used a cubic B-spline to fit the out-of-flare variability, and then removed the fitted B-spline from the light curve. In the residual of a light curve, flares can be detected by residual fluxes larger than 3σ, where σ is the standard deviation of the out-of-flare residual. Finally, the stellar rotational period was calculated from the out-of-flare variability. Detailed steps are as follows:

1. Step 1: Remove the points with fluxes greater than the top 2% flux from the light curve (l_0), the new light curve is denoted as l_1.
2. Step 2: Calculate the Lomb-Scargle periodogram (LS; Lomb 1976; Scargle 1982) of l_1 using the code `LombScargle` in the python package `astropy.timeseries` (Astropy Collaboration et al. 2013, 2018), then determine the period P_0 of the light curve.
3. Step 3: A cubic B-Spline curve with a knot interval of $0.1P_0$ is used to fit the l_1, and denote the new B-Spline as S_1 and $R_1 = l_1 - S_1$. Calculate the standard deviation σ_1 of R_1, and remove the points with R_1 values greater than $2\sigma_1$. The new light curve is denoted as l_2, and $l_1 := l_2$. Then repeat this step again, and obtain the the standard

[8] http://simbad.u-strasbg.fr/Simbad

[9] https://www.aavso.org/vsx/

[10] https://mast.stsci.edu

Table 1
GWAC Flare Stars

#	Name	Other Name	New	R.A. J2000 degree	Decl. J2000 degree	Dis pc	Gmag mag	bp-rp mag	SpT	Multi	Period day	Date yyyymmdd	Start hhmmss	End hhmmss	Flare Energy $\log_{10}$(erg)	ED second
1	TIC 141 533 801	PM J06521 +7908		103.040098	79.14838	39.98	10.514	1.68	M0		5.20898 (0.42182)	20190223	123107	141352	35.09(0.10)	4485
2	TIC 8 688 061	PM J09108 +3127		137.701223	31.45744	27.04	12.506	2.653	M3		4.24599 (0.27568)	20190225	134702	150947	33.6(0.17)	2028
3		HAT 178-02667	Y	131.491539	36.59261	96.88	13.465	2.391	(M2.5)	Binary	1.717885	20190225	134702	150947	34.69(0.47)	4626
4	TIC 253 050 844	G 176-59	Y	177.70409	45.56739	29.6	14.033	3.029	M4.5			20190403	144350	180450	33.82(0.59)	11285
5	TIC 392 402 786	BD+48 1958		174.352417	47.46249	33.47	10.034	1.687	M0	Binary	1.03001 (0.01528)	20190403	144350	180450	34.98(0.09)	1851
6	TIC 416 538 839	StKM 2-809		183.914031	52.65242	25.1	11.373	2.608	M3		0.72597 (0.00680)	20190403	144350	180450	34.3(0.13)	4151
7	TIC 334 637 014	LSPM J1542 +6537		235.554214	65.61809	38.92	13.233	2.889	M4.5		0.61722 (0.00399)	20190403	180612	205708	34.07(0.40)	5561
8	TIC 162 673 744	HAT 149-01951	Y	246.061458	48.39066	59.69	13.615	2.482	M3		1.63170 (0.04786)	20190502	165833	200324	34.22(0.37)	4755
9	TIC 436 680 588	2MASS J04542368 +1709534		73.598678	17.16485	143.62	16.617	2.365	(M2.5)	Binary		20190113	102051	134136	35.37(0.51)	9090
10	TIC 20 161 577	HAT 138-01877	Y	145.345992	43.97308	99.51	12.793	1.78	(M1)		3.13022 (0.14959)	20190125	151425	170400	34.19(0.08)	746
11	TIC 88 723 334	G 196-3	Y	151.089429	50.38705	21.81	10.615	2.35	M2.5		1.31341 (0.02628)	20190125	151425	201525	34.56(0.09)	4946
12	TIC 323 688 555	GJ 3537		137.413115	6.70305	23	12.081	2.629	M3		4.06548 (0.30373)	20190224	135938	153823	33.36(0.10)	1068
13	TIC 318 230 983	HAT 140-00487	Y	162.861825	48.69546	79.05	11.429	1.817	M1		4.06913 (0.25229)	20190124	175515	211330	35.53(0.19)	7433
14		1RXS J075908.2 +171957		119.779882	17.32982	24.16	12.706	2.8	(M4)		0.48204 (0.00411)	20190113	135650	185505	33.5(0.29)	2382
15	EPIC 210 701 183	HAT 307-06930	Y	55.739582	18.37965	132.82	14.414	2.184	M1		1.67409 (0.01648)	20190112	102758	141043	34.75(0.69)	6870
16	TIC 29 172 363	RX J0903.2 +4207		135.811479	42.12356	79.49	11.647	1.703	M0		1.49055 (0.03069)	20190201	170000	193443	35.44(0.13)	7350
17	TIC 283 729 913		Y	63.455228	9.21321	104.41	14.03	2.222	M2.5			20190114	113000	140052	34.36(0.42)	3188
18	TIC 436 614 005	DR Tau		71.775897	16.97856	192.97	11.651	1.621	T Tau			20190114	101252	154952	36.71(0.24)	23321
19	TIC 274 086 357	1RXS J031750.1 +010549	Y	49.457729	1.10221	151.67	12.219	1.38	K3		0.63653 (0.01102)	20181223	125610	162440	35.72(0.29)	6484
20	TIC 427 020 004	HAT 307-01221	Y	49.572707	18.40566	94.92	11.693	1.495	K5		3.16524 (0.22178)	20190111	120004	151035	35.22(0.09)	3200
21	TIC 114 059 158		Y	55.304975	20.85436	140.32	13.862	1.96	M3		0.31366 (0.00193)	20181230	145636	162551	34.88(0.28)	4953
22	TIC 195 188 536	DF Cnc		128.870322	18.20561	49.23	12.906	2.376	M3		5.35280 (0.62707)	20190112	144958	195145	34.11(0.15)	2810
23	TIC 77 644 831	1RXS J101627.8-005127		154.112263	−0.86091	60.15	12.329	2.136	(M1.5)		0.74709 (0.00835)	20190114	155759	191159	34.58(0.11)	3307
24			Y	153.304236	2.80498	105.46	17.593	3.115	(M5)			20190213	170041	180211	34.04(0.27)	1780
25	TIC 374 270 454	1RXS J103715.4 +020612	Y	159.314334	2.09753	71.84	11.829	1.951	M1		3.51123 (0.28641)	20190106	175650	205650	34.59(0.06)	1491

Table 1
(Continued)

#	Name	Other Name	New	R.A. J2000 degree	Decl. J2000 degree	Dis pc	Gmag mag	bp-rp mag	SpT	Multi	Period day	Date yyyymmdd	Start hhmmss	End hhmmss	Flare Energy $\log_{10}$(erg)	ED second
26	TIC 142 877 499	G 236-81		176.772653	70.03285	30.62	13.093	2.856	(M4)	Binary	10.42161 (0.9949)	20190121	153702	205732	34.73(0.54)	16582
27	TIC 142 979 644	1RXS J120656.2 +700754		181.73505	70.13054	17.37	10.892	2.845	(M4)	Binary	4.17903758 (0.00000027)	20190318	134018	190333	33.65(0.12)	1065
28	TIC 103 691 996	G 235-65		154.787606	66.49275	29.26	13.053	2.662	(M3.5)			20190216	164856	195511	34.14(0.37)	9772
29	TIC 99 173 696		Y	123.681926	46.84348	39.3	13.745	2.84	M4		1.78860 (0.01522)	20190206	162410	185425	33.37(0.25)	1733
30	TIC 153 858 162	1RXS J082204.1 +744012		125.533783	74.67285	47.66	12.264	2.266	(M3)		1.97116 (0.05626)	20190121	154417	183817	34.00(0.24)	1297
31	TIC 270 478 293	LP 589-69	Y	34.197584	1.2126	31.51	12.476	2.532	M3		4.49044 (0.33040)	20181224	120134	142234	33.31(0.21)	735
32	TIC 382 379 884		Y	45.066475	−3.04574	114.87	12.073	1.53	M0	Binary	0.45825824 (0.00000316)	20190127	102150	140010	35.48(0.14)	4360
33	TIC 435 308 532	LP 413-19		54.392052	17.85	38.8	12.079	2.712	M3	Binary	0.47630 (0.00278)	20190204	113935	131650	34.12(0.06)	890
34	TIC 440 686 488	V660 Tau		57.116786	23.30076	134.02	12.242	1.319	K5		0.23520 (0.00104)	20190204	113935	131650	35.54(0.24)	5538
35	TIC 457 100 137	1RXS J075554.8 +685514		118.972289	68.9069	29.2	13.056	2.844	(M4)		0.53285 (0.00445)	20			33.18(0.16)	1077
36	EPIC 211 944 670	CU Cnc		127.906559	19.39428	16.65	10.576	2.861	M3.5	Triple	2.7714842 (0.00001076)	20190101	145240	190810	33.96(0.09)	1565
37	TIC 224 304 406	1RXS J123415.2 +481306		188.564232	48.21862	46.83	13.135	2.675	M3		0.94869 (0.01295)	20190206	191205	221635	33.71(0.18)	1535
38		BX Ari		44.546799	20.50087	234.85	11.921	1.541	K3	Binary	2.83690 (0.14557)	20181229	135121	163451	36.35(0.16)	6342
39	TIC 289 040 091	1RXS J064358.4 +704222		100.994199	70.70326	59.56	13.348	2.402	M3		0.54374 (0.00562)	20181215	162100	174019	34.42(0.62)	5981
40	TIC 16 246 712		Y	153.803156	37.86495	95.42	12.945	2.066	M1	Binary		20			34.78(0.14)	1756
41	TIC 445 830 121		Y	173.045411	52.09011	42.3	13.465	2.503	M3	Binary		20190106	210011	222626	33.59(0.48)	1790
42	TIC 197 251 248	G 9-38		134.558692	19.76258	5.15	11.966	3.777	M7	Binary	0.25397 (0.00150)	20190211	150414	155014	32.51(0.15)	1704
43	TIC 316 276 917		Y	133.388088	56.78993	225.65	12.087	1.042	G7		0.65862 (0.00688)	20181227	165728	211943	35.56(0.15)	1797

Note. 1. The bolometric flare energies were calculated from GWAC flares assuming a blackbody with a temperature of 9000 K. The fraction of the bolometric energy in the Gaia G band is $\frac{f_G}{f_{\rm bol}} \approx 0.3$. 2. Spectral types in parentheses are assigned based on $G_{\rm rp} - G_{\rm bp}$. 3. The period of Star #3 is from Hartman et al. (2011).

Table 2
Data of which TESS Sector and K2 Campaign was Used

Star #	Name	Sectors
1	TIC 141 533 801	19,20,26,40
2	TIC 8 688 061	21
3		
4	TIC 253 050 844	22
5	TIC 392 402 786	22
6	TIC 416 538 839	22
7	TIC 334 637 014	14,15,16,17,21,22,23,24,41
8	TIC 162 673 744	23,24,25
9	TIC 436 680 588	(43), (44)
10	TIC 20 161 577	21
11	TIC 88 723 334	21
12	TIC 323 688 555	8,34,45
13	TIC 318 230 983	21
14		44,45,46
15	EPIC 210 701 183	4
16	TIC 29 172 363	21
17	TIC 283 729 913	5,23
18	TIC 436 614 005	(43), (44)
19	TIC 274 086 357	4,31
20	TIC 427 020 004	42,43
21	TIC 114 059 158	42,43,44
22	TIC 195 188 536	44,45
23	TIC 77 644 831	8,35,45
24		
25	TIC 374 270 454	35,45
26	TIC 142 877 499	21
27	TIC 142 979 644	14,15,21,41
28	TIC 103 691 996	14,21,40,41
29	TIC 99 173 696	20
30	TIC 153 858 162	20,26,40,47,53
31	TIC 270 478 293	4,31
32	TIC 382 379 884	(4),31
33	TIC 435 308 532	42,43,44
34	TIC 440 686 488	42,43,44
35	TIC 457 100 137	20,26,40
36	EPIC 211 944 670	5,18
37	TIC 224 304 406	22
38		(42), (43), (44)
39	TIC 289 040 091	19,20,26
40	TIC 16 246 712	21
41	TIC 445 830 121	21, (22)
42	TIC 197 251 248	44,45
43	TIC 316 276 917	20

Note. The TESS sectors in parentheses mean that the data of these sectors are not available for this work.

deviation σ of l_1, B-Spline S, and $R = l_0 - S$ for finding flares.

4. Step 4: A flare is detected from R if there are at least 3 (for curves of 2 minutes cadence) or 2 (for curves of 30 minutes cadence) successive fluxes greater than 2σ and the flare peak is greater than 3σ.
5. Step 5: After all flares were removed from the light curve, the rotational period P was calculated from the out-of-flare light curve by LS.

Figure 1 shows the results of our algorithm. In the upper panel, the red line is the fitted cubic B-spline, and flares detected are shown in blue. All flares detected were inspected by eye, and finally obtained 931 flares.

The rotational periods of 31 stars were obtained by the above algorithm, and the periods of three eclipsing binaries were calculated in Section 4. Star #3 (HAT 178-02667) is not observed by TESS and K2, but it has a period of 1.717 885 days from Hartman et al. (2011), which may be the orbital period (see Section 4 for details), so there are total 35 GWAC flare stars have periods. Among the 31 stars that have rotational periods, 30 stars have periods less than 5.4 days, and the left one has a period of about 10.42 days, and thus all are rapid rotators.

Flares and periods detected in TESS and K2 light curves by the above algorithm, the 43 GWAC flare light curves and the flare movie of Star #4 (G 176-59), #7 LSPM J1542+6537), #28 (G 235-65), and #39 (1RXS J064358.4+704222) are all given in https://nadc.china-vo.org/res/r101145/.

2.2. Flare Energy

The equivalent duration (ED) (Gershberg 1972) was used to calculate a flare energy. ED is defined as: $\sum_i \frac{\triangle f_i}{f} \times \triangle t$, where $\triangle f_i$ is a flux variation at time t_i in the flare, f is the quiescent flux and $\triangle t$ is the cadence. Then the flare energy is $E = \mathrm{ED} \times f$.

GWAC has no filter, and the Gaia G photometry of Gaia DR3 (Gaia Collaboration 2022) was used to calibrate the GWAC photometry by the GWAC pipeline, with a photometric accuracy better than 0.1 mag. Thus, we used the Gaia G band filter and passband zero to calculate the quiescent flux f of a GWAC flare star. The Gaia G band filter was from Riello et al. (2021), the Vega spectrum was from Castelli & Kurucz (1994), and the Gaia G magnitude of Vega was set 0.03 mag (Jordi et al. 2010). As a result, the passband zero p_0 of Gaia G band is 9.12×10^{-6} erg cm^{-2} s^{-1}.

The distances of GWAC flare stars were calculated from parallaxes of Gaia DR3, but there are three stars (Star #8 (HAT 149-01951), #14 (HAT 149-01951), and #29 (HAT 149-01951)) without available parallaxes in Gaia DR3. Then we used the equation of $M_{Ks} = 1.844 + 1.116(V - J)$ given by Raetz et al. (2020), and $d = 10^{0.2(M_{Ks} - Ks - 5)}$ in pc to calculate their distances, where Ks and J are from 2MASS (Skrutskie et al. 2006), and V is from APASS (Henden et al. 2015). As a result, the quiescent flux in the G band of a star is: $f = \pi d^2 p_0 10^{-0.4G}$ erg s^{-1}.

To obtain flare energies of TESS flares, the TESS response function and the passband zero from Sullivan et al. (2017) were used. The observed quiescent flux f_o of a star in the TESS passband was the median value of its light curve multiplied by the TESS passband zero. Thus the quiescent flux is $f = \pi d^2 f_o$.

Two stars: Star #15 (HAT 307-06930) and #36 (CU Cnc) only have K2 light curves. Then the formulae (1)–(6) in

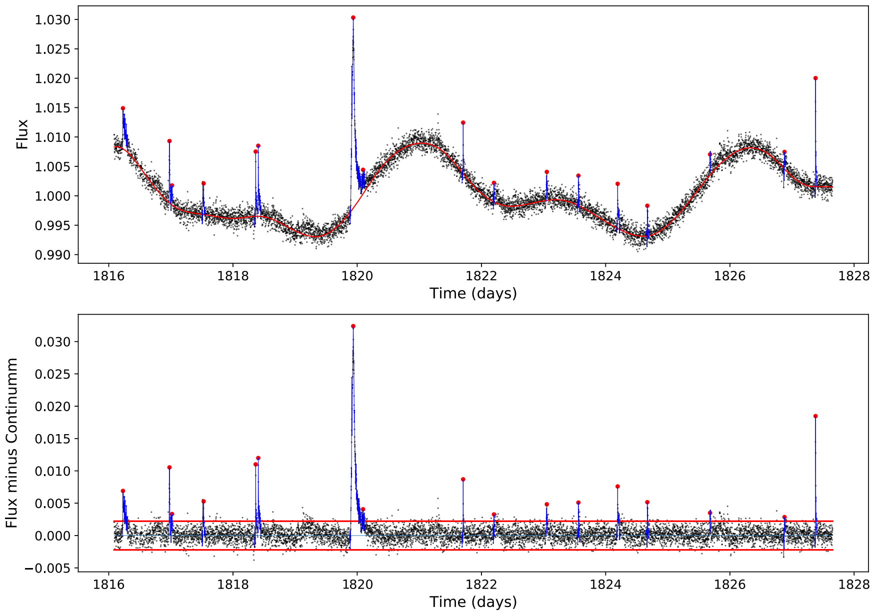

Figure 1. Upper panel: the black dots are from a part of the light curve of Star #1 (TIC 141 533 801) in Sector 19 of TESS. The red curve is the fitted cubic B-Spline curve. Lower panel: the black dots are the residuals of the fluxes minus the fitted cubic B-Spline curve, and the two red lines indicate $\pm 3\sigma$ positions. In both panels, the detected flares are shown in blue lines and their peaks are indicted by red dots.

Shibayama et al. (2013) were used to calculate quiescent fluxes in the Kepler passband,[11] with the surface temperatures and stellar radii from Huber et al. (2016).

We assumed the fare energy was from a blackbody radiation with a temperature of 9000 K, and then used observed flare energies in Gaia G, TESS or K2 filters to calculate whole white light flare energies, which should be lower than the true released flare energies (e.g., Hawley & Pettersen 1991; Kretzschmar 2011).

2.3. Spectra

The Guo Shou Jing Telescope (the Large Sky Area Multi-Object Fiber Spectroscopic Telescope, LAMOST; Cui et al. 2012) can obtain 4000 spectra in one exposure, and is located at the Xinglong Observatory, the same place as GWAC and the 2.16 m telescope. In LAMOST DR8,[12] there are about 11 million low-resolution spectra (LRS, $R \sim 1800$) and 6 million medium-resolution spectra (MRS, $R \sim 7500$). We searched spectra of GWAC flare stars in LAMOST DR8, and obtained available LRS for 25 stars, and MRS for 13 stars. Because 11 stars have available both LAMOST LRS and MRS, there are 27 stars have LAMOST spectra. We also obtained LRS of another seven flare stars by the 2.16 m telescope with the instrument G5. The spectral resolution is about 2.34 Å pixel^{-1}, and the wavelength coverage is 5200 Å–9000 Å (Zhao et al. 2018). In sum, 32 of 43 flare stars have LSR, and 7 have LAMOST MRS.

The spectroscopic standards from Kirkpatrick et al. (1991) were used to assign spectral types of M stars that have LRS from LAMOST or the 2.16 m telescope. For stars that have spectral types earlier than M0, their spectral types are from LAMOST DR8.

The Color-Magnitude Diagram (CMD) of flare stars with their spectra types is shown in Figure 2, where Gaia G, parallax ϖ (in milliarcsecond), $G_{\rm bp} - G_{\rm rp}$ are from Gaia DR3, and the absolute magnitude $M_G = G + 5\log_{10}(\varpi) - 10$. For 32 stars that have LRS, their Hα are all shown in emission, which indicate they are all active stars. Among them, 31 stars were assigned spectral types and are shown in different symbols and colors in Figure 2. Star #21 was assigned a spectral type of M3, but with a bluer color in Figure 2. We found that its ruwe = 2.478 in Gaia DR3, which implies that there may be some astrometric problems or it is not a single star, thus the Gaia photometry is unreliable. Star #18 (DR Tau) is not in Figure 2, because it is a T Tauri star (Chavarria-K. 1979), and there is no available absorption line in its spectrum for spectral classification.

For the other 11 stars without available spectra in this paper, their spectral types were also assigned by their $G_{\rm bp} - G_{\rm rp}$ in Figure 2. Among them, Star #9 (2MASS J04542368+1709534; Herczeg & Hillenbrand 2014), #23 (1RXS J101627.8-005127; Zickgraf et al. 2005), #27 (1RXS J120656.2+700754; Christian et al. 2001), #28 (G 235-65; Reid et al. 2004), #30

[11] The Kepler response function was from https://keplergo.github.io/KeplerSciWebsite/the-kepler-space-telescope.html.
[12] http://www.lamost.org/dr8/v1.1/

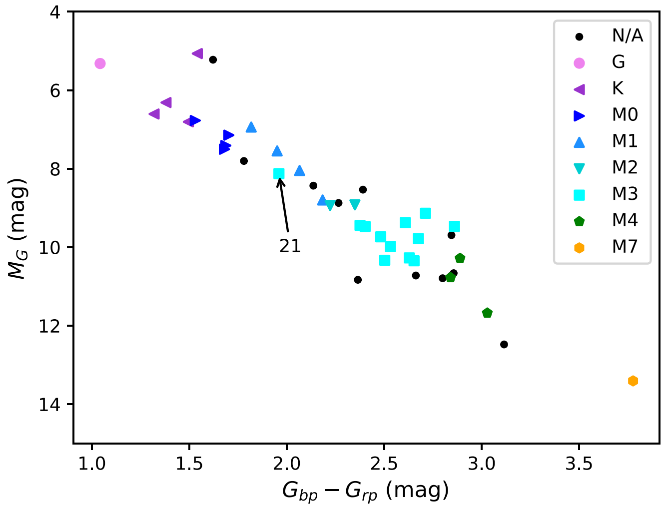

Figure 2. The Color-Magnitude Diagram (CMD) of flare stars with their spectral types. M_G is the absolute magnitude of Gaia G. G, $G_{\rm bp}$ and $G_{\rm rp}$ are from Gaia DR3. The 31 stars that have LRS are shown in different symbols and colors for different spectral types. The black dots are the stars that have not available spectra in this paper.

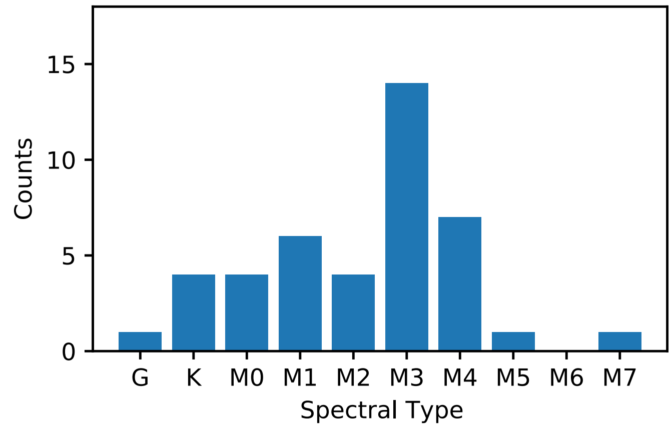

Figure 3. The distribution of spectral types of GWAC flare stars, except one T Tauri (Star #18; DR Tau).

(1RXS J082204.1+744012; Fleming et al. 1988), and #35 (1RXS J075554.8+685514; Zickgraf et al. 2005) had been identified as active stars in the literature.

In sum, there are one G type star, four K type stars, 37 M type stars, and one T Tauri in our sample. Figure 3 shows the distribution of spectral types of GWAC flare stars, except one T Tauri (Star #18; DR Tau).

To calculate the $\rm H_\alpha$ emission luminosity $L_{\rm H_\alpha}$, the Sérsic function (Sersic 1968) was used to fit $\rm H_\alpha$ emission profiles. The function is: $F(\lambda) = A_0 \exp(Z^{A_3}/A_3) + A_4 + A_5\lambda$, where $Z = |(\lambda - A_1)/A_2|$, λ is wavelength in Å, and A_i, $i = 0, \cdots, 5$ are coefficients to be fitted. The wavelength range was set to $6564.61 \pm 20\,\mathring{A}$ (6564.61 Å is the vacuum wavelength of Hα), and the LAMOST spectral luminosity of Hα: $L'_{\rm H_\alpha} = \int_{6544.61}^{6584.61} A_0 \exp(Z^{A_3}\big/A_3)d\lambda$. The fluxes of LAMOST spectra are not calibrated, but there is only a constant ratio between each spectrum and its true flux. For each star that has LAMOST LRS, we calculated its spectral flux f_L from its LRS spectrum in the SDSS r′ filter (Fukugita et al. 1996), and its observed flux f_A from r′ given by APASS (Henden et al. 2015). Then its $L_{\rm H\alpha} = L'_{\rm H\alpha} * f_A/f_L$.

To obtain the quiescent bolometric luminosity $L_{\rm bol}$ of a star, photometric data from r′, g′ and i′ of APASS (Henden et al. 2015), J, H, and K_s of 2MASS (Skrutskie et al. 2006), and W1, W2, W3, and W4 of WISE (Jarrett et al. 2011) for each star, were fitted by a blackbody irradiation function. In the calculation, the reference wavelengths and the zero-points of all filters were from the SVO Filter Profile Service[13] (Rodrigo & Solano 2020). Finally, $L_{\rm H\alpha}/L_{\rm bol}$ can be obtained. $L_{\rm H\alpha}/L_{\rm bol}$ that can be calculated from spectra are listed in Table 3. Because one star can have several LAMOST spectra, and one spectra has one $L_{\rm H\alpha}/L_{\rm bol}$, so there are several $L_{\rm H\alpha}/L_{\rm bol}$ for a star in Table 3.

The information of GWAC flare stars with their GWAC flares is given in Table 1.

[13] http://svo2.cab.inta-csic.es/theory/fps/

3. Flare Profiles

3.1. Sympathetic or Homologous Flares

Based on an enormous amount of observations, solar flares are well known to be produced by magnetic reconnections in active regions (ARs; Toriumi & Wang 2019). Solar ARs are the regions full of intense magnetic fields with complex morphologies (McIntosh 1990; Sammis et al. 2000). Successive flares are often observed on the Sun and are identified as sympathetic activity from different regions with physical causal links (Pearce & Harrison 1990; Moon et al. 2002; Schrijver & Higgins 2015; Hou et al. 2020), or homologous ones occurring in the same AR (e.g., Xu et al. 2014; Louis & Thalmann 2021).

It is interesting that there are three pairs of flares successively appearing among the 43 GWAC samples as shown in Figure 4. Each pair of flares occurred following a similar profile of light curves in the interval of 20–50 minutes. The morphology of the light curves during a flare may reflect the release processes of magnetic energies, and manifest complex magnetic topology of the intense magnetic fields. The successive occurrence of three pairs of stellar flares indicates that the cool stars may share the similar physical magnetic explosions to those sympathetic flares or homologous ones happening on the Sun. With the development of future imaging observations for the other stars, it is anticipated to unveil these possibly universal physical mechanisms.

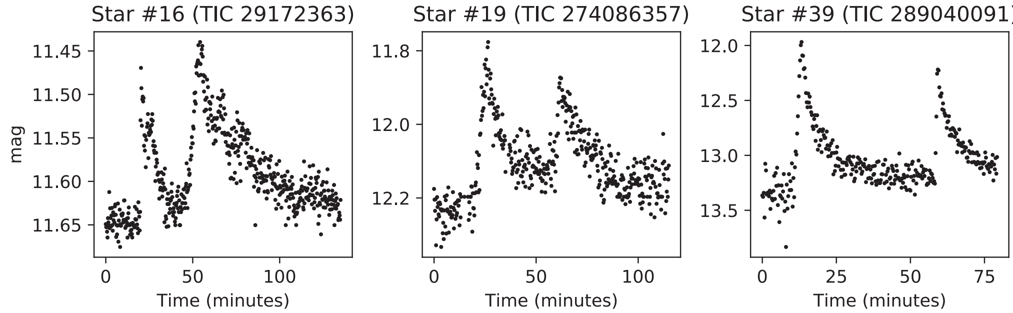

Figure 4. Successive flares from Star #16 (TIC 29 172 363), #19 (TIC 274 086 357; 1RXS J031750.1+010549), and #39 (TIC 289 040 091; 1RXS J064358.4+704222).

Table 3
Hα Luminosity

Star #	R. A. J2000 degree	Decl. J2000 degree	$\lg(L_{\mathrm{H}\alpha}/L)$
2	137.702323	31.457447	−3.78(+0.01), −3.79(+0.01), −3.58(+0.00)
4	177.704090	45.567390	−3.63(+0.01)
5	174.352814	47.462439	−5.05(+0.01)
6	183.914032	52.652434	−3.69(+0.00), −3.68(+0.00), −3.78(+0.01)
7	235.554210	65.618100	−3.15(+0.00)
8	246.061805	48.390525	−3.66(+0.01)
9	73.598465	17.162068	−4.22(+0.02)
11	151.089442	50.387056	−3.67(+0.01), −3.65(+0.00)
12	137.413190	6.703040	−3.63(+0.00), −3.64(+0.00), −3.68(+0.00)
13	162.861881	48.695440	−4.01(+0.01), −4.09(+0.01)
15	55.739577	18.379597	−3.83(+0.01), −3.92(+0.01), −3.94(+0.01)
16	135.811466	42.123555	−3.82(+0.01)
17	63.455420	9.213330	−4.30(+0.01)
18	71.775872	16.978558	−2.47(+0.01), −2.75(+0.01)
19	49.457706	1.102194	−3.80(+0.01)
20	49.572717	18.405648	−4.07(+0.02)
21	55.306192	20.854802	−3.48(+0.00), −4.60(+0.05), −3.56(+0.01), −3.83(+0.02)
22	128.870334	18.205612	−3.84(+0.01), −3.86(+0.01), −3.87(+0.01)
26	159.314354	2.097543	−4.21(+0.03), −4.21(+0.02)
30	123.681884	46.843252	−3.67(+0.00)
32	34.197623	1.212631	−3.94(+0.01)
35	57.116787	23.300774	−3.85(+0.01), −3.82(+0.01)
37	127.906510	19.394273	−3.78(+0.00), −3.76(+0.00), −3.73(+0.00)
38	188.564219	48.218640	−3.74(+0.01), −3.74(+0.01), −3.59(+0.01)
39	44.546799	20.500874	−3.58(+0.01)
40	100.993690	70.702840	−3.69(+0.00), −3.82(+0.01)
41	153.802305	37.864154	−3.76(+0.02), −3.98(+0.05), −3.61(+0.02)

Note. Each spectrum provides one $\lg(L_{\mathrm{H}\alpha}/L)$, with the error in the following parenthesis.

3.2. Quasi-periodic Pulsation

Quasi-periodic pulsations (QPPs) are very common phenomena in solar flares (Kupriyanova et al. 2010; Simões et al. 2015; Van Doorsselaere et al. 2016), but QPPs in stellar white light flares are still rare (Pugh et al. 2016; Howard & MacGregor 2022). More than a dozen of mechanisms were suggested to trigger QPPs (Kupriyanova et al. 2020). Coronal loop lengths can be derived from periods of QPPs from some mechanisms with some theoretical considerations (Ramsay et al. 2021). The periods of QPPs in white light curves are of tens minutes (Pugh et al. 2016; Ramsay et al. 2021), but at short cadence (20 s) of TESS, QPP periods less than 10 minutes were also found (Howard & MacGregor 2022).

GWAC has a cadence of 15 s, shorter than TESS, and make it possible to find QPPs with short periods in GWAC white light flares. One flare occurring on Star #16 (TIC 29 172 363) was found to indicate a QPP process as shown by the red light curve in the left panel of Figure 5. The function $f(t) = A_0 \times \exp(A_1 t) + A_2$ was used to fit the background of the QPP signal, and shown by the blue curve in the left panel of Figure 5. Here, A_0, A_1 and A_2 are parameters to be fitted, and t is time in seconds. According to the light curve after subtracting the background information, a character manifested by QPP process is shown in the middle panel of Figure 5, and is analyzed by using the LS periodogram. The right panel of Figure 5 shows the periodogram result. A period of 13.0 ± 1.5 minutes is obtained for the QPP process.

4. Binary and Multiple Systems

We inspected all GWAC flare stars in Aladin (Bonnarel et al. 2000) and Gaia DR3, and found that there are 11 binaries and one triple system. Among them, Star #27 (TIC 142 979 644; 1RXS J120656.2+700754), #32 (TIC 382 379 884) and #36 (EPIC 211 944 670; CU Cnc) hold close eclipsing binaries. To obtain periods of binaries, we fitted the eclipse minimum times by quadratic polynomials of light curves, and ephemerides

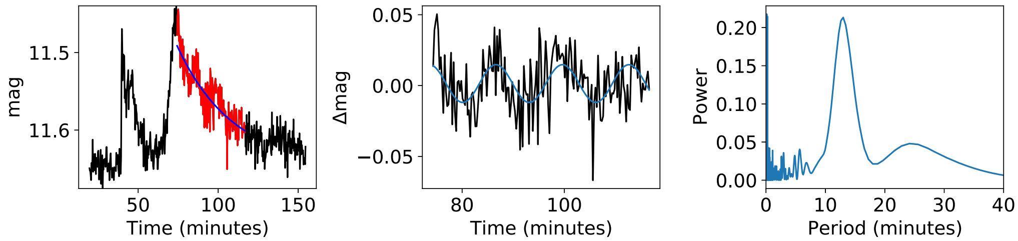

Figure 5. The QPP of Star #16 (TIC 29 172 363). Left panel: the QPP position in the flare is indicated in red. The blue curve is the fitted background. Middle panel: the QPP signal without background. The blue curve is the fitted QPP with a period of 13.0 minutes; Right panel: the LS periodogram of the QPP signal in the middle panel.

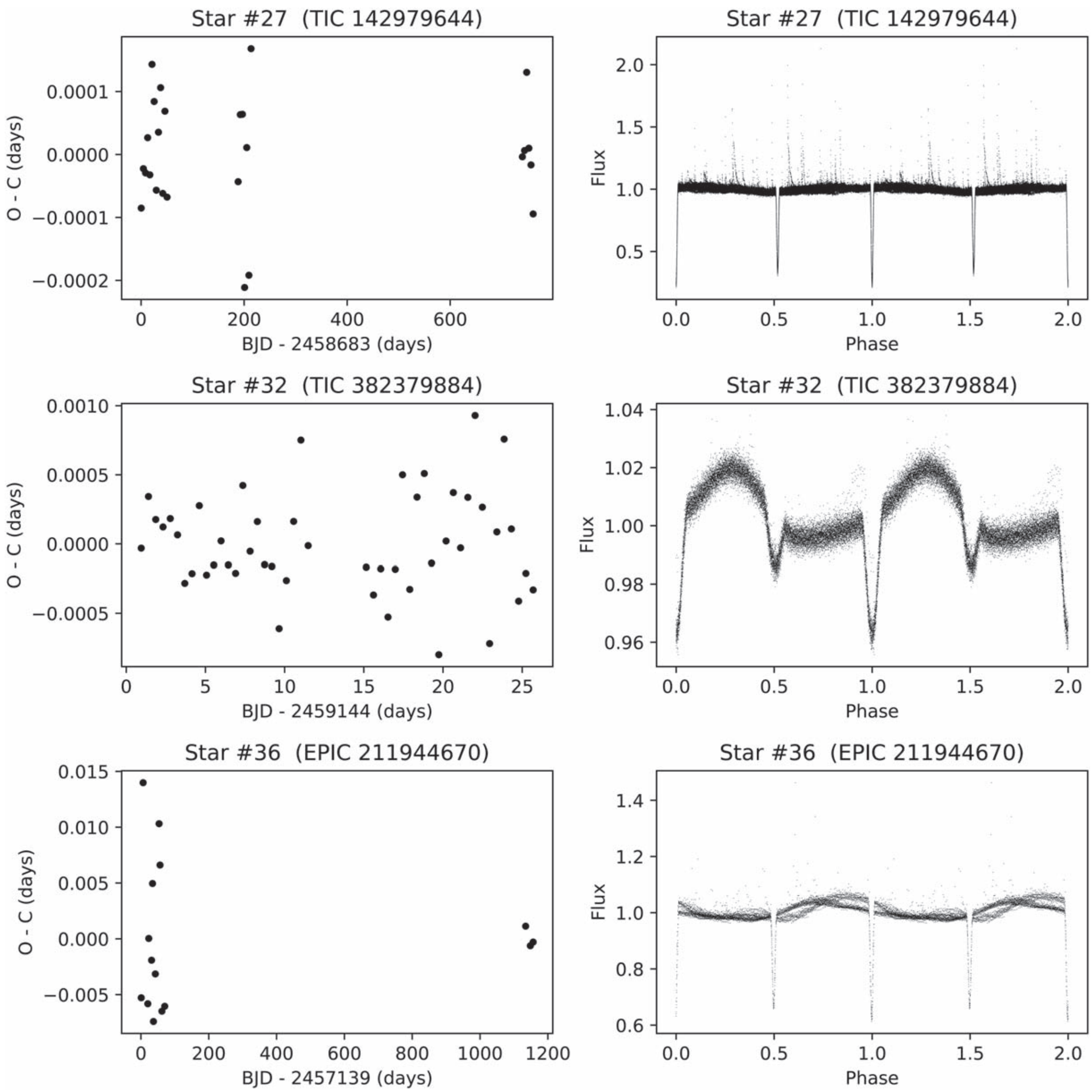

Figure 6. O–C diagrams and light curves in phases of Star #27 (TIC 142 979 644; 1RXS J120656.2+700754), #32 (TIC 382 379 884) and #36 (EPIC 211 944 670; CU Cnc) are shown in the left and right columns, respectively.

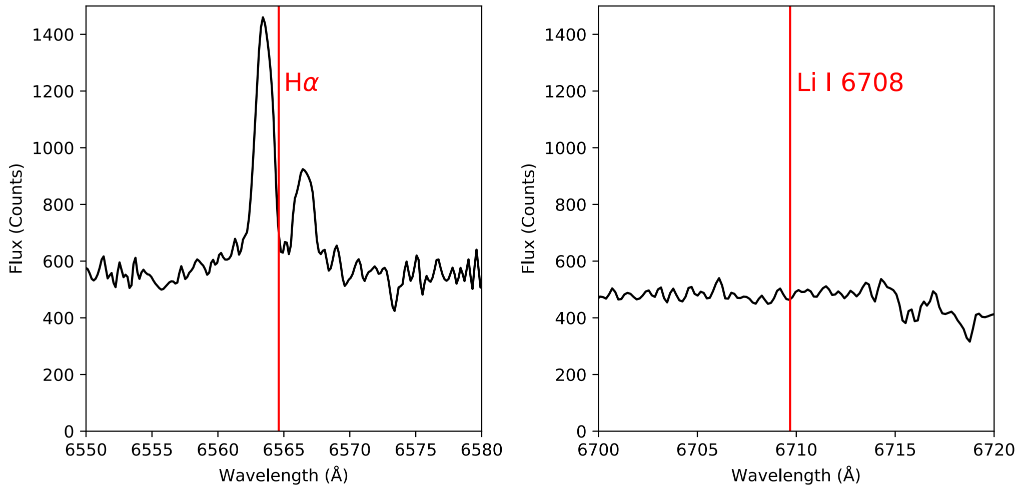

Figure 7. The LAMOST MRS of Star #3 (HAT 178-02667). Left panel: Double Hα emissions of Star #3 (HAT 178-02667); Right panel: There is no Li I 6708. The positions of Hα and Li I 6708 in vacuum are indicated in red lines.

were calculated by fitting the eclipse minimum times. The ephemerides (in BJD) of Star #27 (TIC 142 979 644; 1RXS J120656.2+700754), #32 (TIC 382 379 884) and #36 (EPIC 211 944 670; CU Cnc) are

$$T_{\min} - 2\,457\,000 = 1683.36653104(\pm 0.000\,023\,99) + 4.179\,037\,58(\pm 0.000\,000\,27)E,$$

$$T_{\min} - 2\,457\,000 = 2144.48865796(\pm 0.000\,103\,48) + 0.458\,258\,24(\pm 0.000\,003\,16)E,$$

and

$$T_{\min} - 2\,454\,833 = 2306.95408506(\pm 0.001\,994\,51) + 2.771\,471\,42(\pm 0.000\,010\,76)E,$$

respectively. Here, E is the circle number, and $T_{\min}$ is the eclipse minimum time. O–C diagrams and light curves in phase are shown in Figure 6. Star #36 (EPIC 211 944 670; CU Cnc) is a triple system in Gaia DR3, so its ephemerides may be disturbed by the third star.

The secondary eclipse minimum of Star #27 (TIC 142 979 644; 1RXS J120656.2+700754) deviates from the phase 0.5 in Figure 6, so it has an eccentricity. We used formulae 1 and 2 in Lei et al. (2022) to calculate its eccentricity (e) and periastron angle (ω). From our calculation, its secondary eclipse phase $\phi_2 = 0.518$ (its primary eclipse phase $\phi_1 = 0$), and the widths of the primary and secondary eclipses were determined by eye, which are $w_1 \sim 0.0176$ and $w_2 \sim 0.018$, respectively. Then, $e\cos(\omega) = \frac{\pi}{2}[\phi_2 - \phi_1 - 0.5] = 0.028\,274$ and $e\sin(\omega) = \frac{w_2 - w_1}{w_2 + w_1} \sim 0.011\,236$. As a result, $e \sim 0.03$ and $\omega \sim 0.387$.

Star #3 (HAT 178-02667) has no Li I 6708 line in its LAMOST MRS as shown in the right panel of Figure 7, which implies that it is not a young star, and thus it unlikely holds a curcumstellar disk. Its ruve = 7.65 in Gaia DR3 and there are

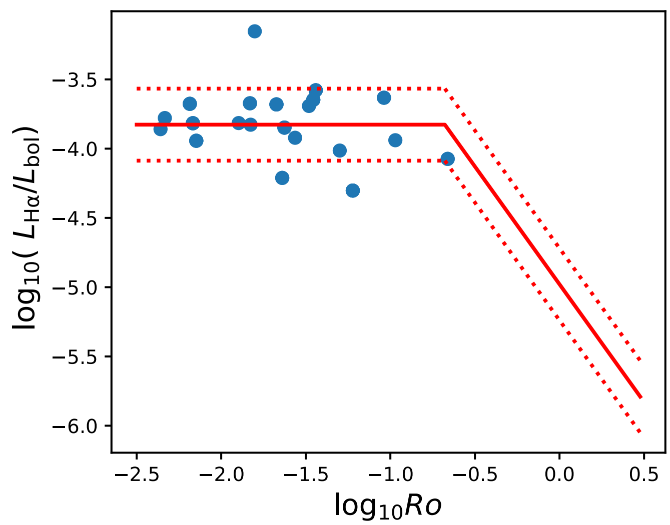

Figure 8. The relationship between Ro and $L_{\mathrm{H}\alpha}/L_{\mathrm{bol}}$. The red line and dotted lines are the relationship and 1σ contours given in (Newton et al. 2017).

double Hα emissions in its LAMOST MRS as shown in the left panel of Figure 7, so it is likely a binary system and double Hα emissions indicate that both components are active stars. In Hartman et al. (2011), it has a period of 1.717 885 days.

5. Hα

Hα is a very important indicator of stellar activity. Stars with strong Hα emissions in their quiescent spectra are very likely to show strong flare activities (Kowalski et al. 2009). Figure 8 shows the relationship between Hα luminosity from 44 spectra of 21 M dwarfs and $Ro = P_{\mathrm{rot}}/\tau$, where P_{rot} is the stellar rotational period and τ is the convective turnover time calculated from Equation (10) in Wright et al. (2011). For M

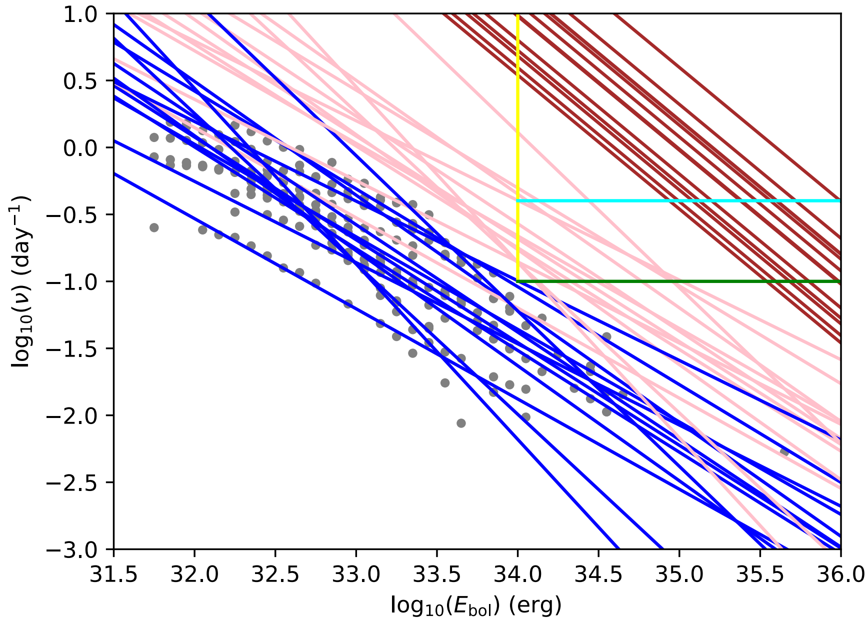

Figure 9. FFDs of 13 flaring single stars with flare numbers greater than 20. The gray dots are the flare frequency obtained from TESS or K2 light curves, and their fitted power law functions are shown by blue lines for a flare temperature of 9000 K, while pink lines for 30,000 K. The yellow line is log $_{10}(E_{\rm bol}) = 34$, and $\nu = 0.1$ and 0.4 are shown in cyan and green lines, respectively. The brown lines represent the abiogenesis zones for flare stars calculated by Equation (10) in Günther et al. (2020).

type stars, their $L_{\rm X}/L_{\rm bol}$ shows saturation (e.g., Pizzolato et al. 2003; Wright et al. 2018) and even supersaturation (e.g., Jeffries et al. 2011) for rapid rotators. Compared to Figure 7 in Newton et al. (2017), our sample stars are all rapid rotators, and in the saturation region as shown In Figure 8.

6. Habitability

Stellar activity is a double-edged sword for life on a habitable planet. On one hand, flare activities can contribute the generation and development of life (Rimmer et al. 2018), on the other hand erode and even destroy the ozone of a habitable-zone exoplanet (Tilley et al. 2019). We used Equation (10) in Günther et al. (2020) to delineate "abiogenesis zone," which means the flare frequency in this zone can contribute the prebiotic chemistry and then promote life generation.

The flare frequency distribution (FFD) is the cumulative flare energy frequency in per day (Gershberg 1972; Günther et al. 2020), and often used to show how often a flare energy higher than a given value is. We obtained FFDs of 13 single stars with more than 20 flares detected in TESS or K2 light curves, and a power law function $\log_{10}(\nu) = \alpha \log_{10}(E_{\rm bol}) + \beta$ was used to fit each FFD, where ν is the cumulative flare frequency in day^{-1}, $E_{\rm bol}$ is the flare energy in erg, α and β are parameters to be fitted. We also calculated the flare frequency ν of the GWAC flare energy using the fitted α and β for each star, and found GWAC flares can occur at a frequency of 0.5 to 9.5 yr^{-1}.

Flares with $E_{\rm bol} \geqslant 10^{34}$ erg can impact atmospheres of habitable planets. The cumulative flare frequency of $\nu \geqslant 0.4$ day^{-1} can remove more than 99.99% of the ozone layer of a habitable-zone exoplanet as suggested by Tilley et al. (2019), and a more permissive frequency limit is $\nu \geqslant 0.1$ day^{-1}. Though the flare temperature of 9000 K is popularly used in literature, but the flare temperature can reach as high as 30,000 K and even 42,000 K (Howard et al. 2020b). In Figure 9, blue lines for a flare temperature of 9000 K, while pink lines for 30,000 K. We can see that for the flare temperature of 9000 K, two stars (TIC 88 723 334 and TIC 416 538 839) produce flares with energies greater than 10^{34} erg in the highest frequencies, but still cannot destroy ozone layers of their habitable planets. However, for the flare temperature 30,000 K, almost all stars can produce energetic flares to destroy ozone layers of their habitable planets, except Star #28 (TIC 103 691 996).

Equation (10) in Günther et al. (2020) was also used to calculate the flare frequency limit for prebiotic chemistry. These frequency limits are shown by brown lines in Figure 9, and there is no star having enough high energetic flares to trigger prebiotic chemistry on its habitable planets.

7. Conclusion

In this paper, we studied the 43 flares from 43 stars found in the GWAC archive between 2018 December and 2019 May, by combining light curves from TESS and K2, spectra from LAMOST and the 2.16 m telescope at the Xinglong Observatory, and parallax and photometry from Gaia DR3, and obtained the following results:

1. We found 19 new active stars.
2. We found three sympathetic or homologous flares, which imply that the cool stars may share the similar physical magnetic explosions to those happening on the Sun.
3. We found a white light QPP in the sympathetic or homologous flare of Star #16 (RX J0903.2+4207) with a period of 13.0 ± 1.5 minutes, which shows the advantage of GWAC with a cadence of 15 s in discovering white light QPPs with short periods.
4. Thirty-four stars have rotational or orbital periods less than 5.4 days and only one star has a period of $\sim$10.42 days.
5. Eleven stars are binaries and one is a triple system. The ephemerides of three binaries are calculated from their light curves, and one of them (Star #27; 1RXS J120656.2+700754) also has an eccentricity of $e \sim 0.03$. Star #3 (HAT 178-02667) has no light curve, but double Hα emissions in its LAMOST medium-resolution spectrum imply a binary.
6. $L_{\mathrm{H}\alpha}/L_{\mathrm{bol}}$ shows that the rapid rotators in GWAC flare stars are in the saturation region in the rotation-activity diagram.
7. Some of GWAC flare stars may produce enough energetic flares to destroy the ozone layer, but none can trigger prebiotic chemistry on its habitable planet.

Big flares with amplitudes greater than 1 mag detected by GWAC, can trigger telescopes in the Xinglong Observatory to follow up. Some research results have been obtained based on these observations (Wang et al. 2021; Xin et al. 2021; Wang et al. 2022). In future, we will continue to analyse these big flares to study their generation mechanisms and impacts on habitable planets.

Acknowledgments

We thank our anonymous referee for the insightful comments. This work is supported by the National Natural Science Foundation of China (NSFC) with grant No. 12073038. This work is supported by the Joint Research Fund in Astronomy U1931133 under cooperative agreement between the National Natural Science Foundation of China (NSFC) and Chinese Academy of Sciences (CAS). Chen Yang, Chao-Hong Ma, Xu-Kang Zhang, Xin-Li Hao, and Xiao-Feng Meng acknowledge the NSFC with grant No. 61941121. Jie Chen acknowledges the Beijing Natural Science Foundation, No. 1222029.

Guang-Wei Li thanks Dr. Ting Li for helpful discussions.

Guo Shou Jing Telescope (the Large Sky Area Multi-Object Fiber Spectroscopic Telescope LAMOST) is a National Major Scientific Project built by the Chinese Academy of Sciences, Funding for the project has been provided by the National Development and Reform Commission. LAMOST is operated and managed by the National Astronomical Observatories, Chinese Academy of Sciences.

We acknowledge the support of the staff of the Xinglong 2.16 m telescope. This work was partially supported by the Open Project Program of the Key Laboratory of Optical Astronomy, National Astronomical Observatories, Chinese Academy of Sciences.

This research has made use of “Aladin sky atlas” developed at CDS, Strasbourg Observatory, France.

ORCID iDs

Guang-Wei Li (李广伟) https://orcid.org/0000-0001-7515-6307
Jie Chen (陈洁) https://orcid.org/0000-0001-7472-5539
Li-Ping Xin (辛立平) https://orcid.org/0000-0002-9422-3437
Xin-Li Hao (郝新丽) https://orcid.org/0000-0001-5770-4218
Xiao-Feng Meng (孟小峰) https://orcid.org/0000-0002-7889-2120

References

Astropy Collaboration, Price-Whelan, A. M., Sipőcz, B. M., et al. 2018, AJ, 156, 123
Astropy Collaboration, Robitaille, T. P., Tollerud, E. J., et al. 2013, A&A, 558, A33
Atri, D., & Mogan, S. R. C. 2021, MNRAS, 500, L1
Bai, T., & Sturrock, P. A. 1989, ARA&A, 27, 421
Balona, L. A. 2015, MNRAS, 447, 2714
Bonnarel, F., Fernique, P., Bienaymé, O., et al. 2000, A&AS, 143, 33
Borucki, W. J., Koch, D., Basri, G., et al. 2010, Sci, 327, 977
Caldwell, D. A., Tenenbaum, P., Twicken, J. D., et al. 2020, RNAAS, 4, 201
Castelli, F., & Kurucz, R. L. 1994, A&A, 281, 817
Chavarria-K., C. 1979, A&A, 79, L18
Christian, D. J., Craig, N., Dupuis, J., Roberts, B. A., & Malina, R. F. 2001, AJ, 122, 378
Colombo, S., Orlando, S., Peres, G., et al. 2019, A&A, 624, A50
Cui, X.-Q., Zhao, Y.-H., Chu, Y.-Q., et al. 2012, RAA, 12, 1197
Davenport, J. R. A., Covey, K. R., Clarke, R. W., et al. 2019, ApJ, 871, 241
De Pontieu, B., Polito, V., Hansteen, V., et al. 2021, SoPh, 296, 84
Fleming, T. A., Liebert, J., Gioia, I. M., & Maccacaro, T. 1988, ApJ, 331, 958
Fukugita, M., Ichikawa, T., Gunn, J. E., et al. 1996, AJ, 111, 1748
Gaia Collaboration 2022, VizieR Online Data Catalog, I/355
Gallet, F., & Bouvier, J. 2013, A&A, 556, A36
Gershberg, R. E. 1972, Ap&SS, 19, 75
Günther, M. N., Zhan, Z., Seager, S., et al. 2020, AJ, 159, 60
Hartman, J. D., Bakos, G. Á., Noyes, R. W., et al. 2011, AJ, 141, 166
Hawley, S. L., & Pettersen, B. R. 1991, ApJ, 378, 725
Henden, A. A., Levine, S., Terrell, D., & Welch, D. L. 2015, AAS Meeting, 225, 336.16
Herczeg, G. J., & Hillenbrand, L. A. 2014, ApJ, 786, 97
Hou, Y. J., Li, T., Song, Z. P., & Zhang, J. 2020, A&A, 640, A101
Howard, W. S., Corbett, H., Law, N. M., et al. 2020a, ApJ, 895, 140
Howard, W. S., Corbett, H., Law, N. M., et al. 2020b, ApJ, 902, 115
Howard, W. S., & MacGregor, M. A. 2022, ApJ, 926, 204
Huber, D., Bryson, S. T., Haas, M. R., et al. 2016, ApJS, 224, 2
Ilin, E., Schmidt, S. J., Poppenhäger, K., et al. 2021, A&A, 645, A42
Jackman, J. A. G., Wheatley, P. J., Acton, J. S., et al. 2021, MNRAS, 504, 3246
Jarrett, T. H., Cohen, M., Masci, F., et al. 2011, ApJ, 735, 112
Jeffries, R. D., Jackson, R. J., Briggs, K. R., Evans, P. A., & Pye, J. P. 2011, MNRAS, 411, 2099
Jenkins, J. M., Twicken, J. D., McCauliff, S., et al. 2016, Proc. SPIE, 9913, 99133E
Jordi, C., Gebran, M., Carrasco, J. M., et al. 2010, A&A, 523, A48
Kahler, S. W. 1992, ARA&A, 30, 113
Kirkpatrick, J. D., Henry, T. J., & McCarthy, D. W. J. 1991, ApJS, 77, 417

Kowalski, A. F., Hawley, S. L., Hilton, E. J., et al. 2009, AJ, 138, 633
Kretzschmar, M. 2011, A&A, 530, A84
Kupriyanova, E. G., Melnikov, V. F., Nakariakov, V. M., & Shibasaki, K. 2010, SoPh, 267, 329
Kupriyanova, E., Kolotkov, D., Nakariakov, V., & Kaufman, A. 2020, STP, 6, 3
Lammer, H., Lichtenegger, H. I. M., Kulikov, Y. N., et al. 2007, AsBio, 7, 185
Law, N. M., Fors, O., Ratzloff, J., et al. 2015, PASP, 127, 234
Lei, Y., Li, G., Zhou, G., & Li, C. 2022, AJ, 163, 235
Li, T., Chen, A., Hou, Y., et al. 2021, ApJL, 917, L29
Lin, R. P., Dennis, B. R., Hurford, G. J., et al. 2002, SoPh, 210, 3
Lomb, N. R. 1976, Ap&SS, 39, 447
Louis, R. E., & Thalmann, J. K. 2021, ApJL, 907, L4
Lu, H.-p., Zhang, L.-y., Shi, J., et al. 2019, ApJS, 243, 28
Ma, X. B. 2019, Fuzzy Matching based Anomaly Pattern Detection in Light Curve Time Series, Master's thesis, Tsinghua Univ.
McIntosh, P. S. 1990, SoPh, 125, 251
Moon, Y. J., Choe, G. S., Park, Y. D., et al. 2002, ApJ, 574, 434
Newton, E. R., Irwin, J., Charbonneau, D., et al. 2017, ApJ, 834, 85
Osten, R. A., Hawley, S. L., Allred, J. C., Johns-Krull, C. M., & Roark, C. 2005, ApJ, 621, 398
Paudel, R. R., Gizis, J. E., Mullan, D. J., et al. 2020, MNRAS, 494, 5751
Pearce, G., & Harrison, R. A. 1990, A&A, 228, 513
Pesnell, W. D., Thompson, B. J., & Chamberlin, P. C. 2012, SoPh, 275, 3
Pizzolato, N., Maggio, A., Micela, G., Sciortino, S., & Ventura, P. 2003, A&A, 397, 147
Pugh, C. E., Armstrong, D. J., Nakariakov, V. M., & Broomhall, A. M. 2016, MNRAS, 459, 3659
Qian, S. B., Zhang, J., He, J. J., et al. 2018, ApJS, 235, 5
Raetz, S., Stelzer, B., Damasso, M., & Scholz, A. 2020, A&A, 637, A22
Ramsay, G., Kolotkov, D., Doyle, J. G., & Doyle, L. 2021, SoPh, 296, 162
Reid, I. N., Cruz, K. L., Allen, P., et al. 2004, AJ, 128, 463
Ricker, G. R., Winn, J. N., Vanderspek, R., et al. 2015, JATIS, 1, 014003
Riello, M., De Angeli, F., Evans, D. W., et al. 2021, A&A, 649, A3
Rimmer, P. B., Xu, J., Thompson, S. J., et al. 2018, SciA, 4, eaar3302
Rodrigo, C., & Solano, E. 2020, XIV.0 Scientific Meeting (virtual) of the Spanish Astronomical Society, 182
Rodríguez Martínez, R., Lopez, L. A., Shappee, B. J., et al. 2020, ApJ, 892, 144
Sammis, I., Tang, F., & Zirin, H. 2000, ApJ, 540, 583
Scargle, J. D. 1982, ApJ, 263, 835
Schrijver, C. J., & Higgins, P. A. 2015, SoPh, 290, 2943
Sersic, J. L. 1968, Atlas de Galaxias Australes
Shappee, B. J., Prieto, J. L., Grupe, D., et al. 2014, ApJ, 788, 48
Shibayama, T., Maehara, H., Notsu, S., et al. 2013, ApJS, 209, 5
Simões, P. J. A., Hudson, H. S., & Fletcher, L. 2015, SoPh, 290, 3625
Skrutskie, M. F., Cutri, R. M., Stiening, R., et al. 2006, AJ, 131, 1163
Sullivan, P. W., Winn, J. N., Berta-Thompson, Z. K., et al. 2017, ApJ, 837, 99
Tilley, M. A., Segura, A., Meadows, V., Hawley, S., & Davenport, J. 2019, AsBio, 19, 64
Toriumi, S., & Wang, H. 2019, LRSP, 16, 3
Tu, Z.-L., Yang, M., Wang, H. F., & Wang, F. Y. 2021, ApJS, 253, 35
Van Doorsselaere, T., Kupriyanova, E. G., & Yuan, D. 2016, SoPh, 291, 3143
Vida, K., Oláh, K., Kővári, Z., et al. 2019, ApJ, 884, 160
Wang, J., Li, H. L., Xin, L. P., et al. 2020, AJ, 159, 35
Wang, J., Li, H. L., Xin, L. P., et al. 2022, ApJ, 934, 98
Wang, J., Xin, L. P., Li, H. L., et al. 2021, ApJ, 916, 92
Wei, J., Cordier, B., Antier, S., et al. 2016, arXiv:1610.06892
Wheatley, P. J., West, R. G., Goad, M. R., et al. 2018, MNRAS, 475, 4476
Wright, N. J., Drake, J. J., Mamajek, E. E., & Henry, G. W. 2011, ApJ, 743, 48
Wright, N. J., Newton, E. R., Williams, P. K. G., Drake, J. J., & Yadav, R. K. 2018, MNRAS, 479, 2351
Xin, L. P., Li, H. L., Wang, J., et al. 2021, ApJ, 909, 106
Xu, J., Ritson, D. J., Ranjan, S., et al. 2018, Chem. Commun., 54, 5566
Xu, Y., Jing, J., Wang, S., & Wang, H. 2014, ApJ, 787, 7
Yakut, K., & Eggleton, P. P. 2005, ApJ, 629, 1055
Yang, H., & Liu, J. 2019, ApJS, 241, 29
Yang, H., Liu, J., Gao, Q., et al. 2017, ApJ, 849, 36
Zhang, J., Bi, S., Li, Y., et al. 2020, ApJS, 247, 9
Zhao, Y., Fan, Z., Ren, J.-J., et al. 2018, RAA, 18, 110
Zickgraf, F. J., Krautter, J., Reffert, S., et al. 2005, A&A, 433, 151
Zweibel, E. G., & Yamada, M. 2009, ARA&A, 47, 291